TITLE: Altered Bone Mechanics, Architecture and Composition in the Skeleton of TIMP-3-Deficient Mice

AUTHORS: Brendyn Miller, Lyudmila Spevak, Lyudmila Lukashova, Behzad Javaheri, Andrew A. Pitsillides, Adele Boskey, George Bou-Gharios, Alessandra Carriero

JOURNAL TITLE: Calcified Tissue International

PUBLICATION DATE: June 2017

PUBLISHER: Springer Verlag

DOI: 10.1007/s00223-017-0248-5

Altered bone architecture, composition and mechanics in the skeleton of TIMP-3 deficient mice

Authors: Brendyn Miller[1], Lyudmila Spevak[2], Lyudmila Lukashova[2], Behzad Javaheri[3], Andrew A. Pitsillides[3], Adele Boskey[2], George Bou-Gharios[4], and Alessandra Carriero[1*]

Affiliations:

[1]Department of Biomedical Engineering, Florida Institute of Technology, USA

[2]Hospital for Special Surgery, USA

[3]Department of Comparative Biomedical Sciences, Royal Veterinary College, London, UK

[4]Institute of Aging and Chronic Disease, University of Liverpool, UK

* Corresponding author: Dr. Alessandra Carriero, Department of Biomedical Engineering, Florida Institute of Technology, 150 West University Boulevard, Melbourne, FL 32901, USA. email: acarriero@fit.edu; tel: +1-321-674-8494

Abstract: Tissue inhibitor of metalloproteinases-3 (TIMP-3) maintains a healthy extracellular matrix by regulating activity of matrix metalloproteinases (MMP), disintegrin-metalloproteinases (ADAM), and disintegrin and metalloproteinases with ThromboSpondin-like motifs (ADAMTS) activity. Currently, there is a need for a comprehensive understanding of the effects of TIMP-3 on bone quality and quantity. In this study, we examined the mechanical, morphological, and compositional properties of TIMP-3 knock out (*Timp-3*$^{-/-}$) mouse bone. We hypothesize that the lack of TIMP-3 plays an important role in maintaining the overall bone integrity. Mechanical properties of humeri, lumbar vertebrae and femurs from *Timp-3*$^{-/-}$ mice were determined using 3-point bending, compression, and notched 3-point bending testing, respectively. Morphological properties of the humeral cortical and trabecular bone and the caudal vertebrae cortical bone were evaluated using micro-computed tomography, while the composition of the femoral cortical and trabecular bone was examined using Fourier transform infrared spectroscopic imaging. Our results revealed that the mechanical integrity of the *Timp-3*$^{-/-}$ bone is compromised due to changes in its composition, structure, and mechanics. Reductions in the yield and ultimate load and stress capacity, and loss in toughness were attributed to reduced bone density and thickness, and increased porosity of cortical bone. Thin trabeculae were dense, highly connected and closely packed in *Timp-3*$^{-/-}$ bone. Furthermore, altered cortical and trabecular bone mineralization and increased compositional heterogeneity were found in *Timp-3*$^{-/-}$ bone, all being indicative of high bone remodelling. In conclusion, this study suggests that TIMP-3 serves a crucial role in normal bone development and maintenance.

Keywords: tissue inhibitor of metalloproteinase-3, bone strength, bone fracture, bone tissue mineral density, bone structure, bone composition

1. Introduction

Tissue Inhibitor of Metalloproteinases-3 (TIMP-3) is one of the four members of the TIMP family of proteins, which primarily inhibits the activity of matrix metalloproteinases (MMP) in the extracellular matrix (ECM). The TIMPs are comprised of 184 to 194 amino acids, whose N-terminal domain allows the protein to bind to the MMPs with a 1:1 molar stoichiometric ratio and prevents these proteinases from cleaving components of the ECM [1]. All the TIMPs inhibit MMPs, but they have different specificities. TIMP-1 has been shown to be ineffective at inhibiting MMP-14, MMP-16, MMP-19, and MMP-24, while TIMP-2 and TIMP-3 are less effective than TIMP-1 at inhibiting MMP-3 and MMP-7 [1]. TIMP-3 is particularly effective at inhibiting MMP-1 and -2, and the membrane-bound MMPs (MMP-14, -15, -16, -17, -24, and -25) [1, 2]. Among the four TIMPs, TIMP-3 is the only one to additionally inhibit a large variety of disintegrin–metalloproteinases (ADAM, particularly ADAM-10, -12, -17, -28, and -33) and disintegrin–metalloproteinases with ThromboSpondinlike motifs (ADAMTS, principally ADAMTS-1, -4, and -5), which help direct cell functions such as proliferation and migration [1, 3, 4]. Due to its role in regulating MMP, ADAM, and ADAMTS activity and its unique property to reside exclusively in the ECM, TIMP-3 may strongly influence hematopoiesis and ECM remodeling [5]. Studies investigating the effects of TIMP-3 on different types of biological tissue have determined that the lack of TIMP-3 results in adverse tissue formation [6] and pathological disorders, which include periodontitis [7], oral squamous cell carcinoma [7], and Sorsby's fundus dystrophy [8] in humans. TIMP-3-deficient mice (*Timp-3*$^{-/-}$) further exhibited increased collagen degradation [9], exacerbated inflammatory process [10], osteoarthritis [9], high angiogenesis [6], abnormal vascularization [11], dilated

cardiomyopathy [12], increased bronchiole branching [13], severe diabetic symptoms [14], failed liver regeneration [10], and tumor growth [6, 12]. Recent studies of *Timp-3*$^{-/-}$ bone found that they are small in size, with compromised mass and structure, and increased number of osteoclasts [15].

This body of research shows that TIMP-3 is crucial for maintaining tissue integrity and suggests that the lack of TIMP-3 can adversely affect skeletal ECM, possibly by disrupting the process of bone remodeling due to unregulated MMP, ADAM, and ADAMTS activity. However, there is a need for a more comprehensive understanding of the influence of TIMP-3 on bone quality and integrity. Specifically, how is TIMP-3 deficiency affecting the mechanics of bone? How are structure and composition of TIMP-3-deficient bone contributing to its mechanical properties? How are these affecting the function of bone? In this study, we analyze the bones from the *Timp-3*$^{-/-}$ mouse model [16], measure bone strength in compression and bending, and bone fracture toughness at the whole organ level. To explain changes in the mechanical properties of the *Timp-3*$^{-/-}$ bone, we examine its morphology at the microscale length and determine the contribution of TIMP-3 to the bone mineral and collagen arrangement at the tissue level. Understanding how mechanical, structural, and compositional properties of cortical and trabecular bone change in *Timp-3*$^{-/-}$ mice provide insights into the role of TIMP-3 in bone development and maintenance.

2. Materials and Methods

Bones from 8-week-old female mice genetically deficient in TIMP-3 (*Timp-3*$^{-/-}$, $N = 9$) and their wild-type (WT) C57BL6 ($N = 6$) littermates were analyzed [16]. Only fresh frozen mice were available at the beginning of this study. They were obtained from a local colony

that was maintained in accordance with the Home Office (UK) guidelines for the care and use of laboratory animals. Mice were stored at −20 °C after euthanasia. Prior to testing, bones were dissected from the fresh frozen mice, cleaned of soft tissue, wrapped in physiological solution (PBS)-soaked gauze, and stored at 25 °C until testing (less than 12 h).

Bone Strength

The right humeri and L5 vertebrae from WT and *Timp-3*$^{-/-}$ mice were loaded to fracture in three-point bending and compression, respectively, using a 50 N load cell (Instron 5866, Norwood, MA) [17]. Humeri were loaded at their mid-diaphysis in the anterior–posterior direction with a displacement rate of 1 μm s−1 at 25 °C in PBS-irrigated conditions. Force–deflection curves were analyzed with a custom program (Matlab, MathWorks) to measure the bone stiffness (S, slope of the linear elastic deformation), yield force (F_y, force limit between the elastic and plastic deformation, defined as the intersection point between the 0.2% linear offset curve and the force–displacement curve), ultimate force (F_u, maximum force), work to yield (W_y, area under the force–displacement curve up to the yield point), and work to fracture (W_f, area under the force–displacement curve up to bone rupture) [17].

Humeri

Prior to mechanical testing, geometrical parameters, i.e., mid-humeral diameter (D), cross-sectional area (CSA), and second moment of inertia (I_{min}) were measured from microcomputed tomography (μCT) images of the humeral middiaphysis (Table 1). Cortical bone was scanned along the long axis of humeri using SkyScan1172 (5 μm voxel size,

55 kVp, 0.36 degrees rotation step (180 degrees angular range), 200 μA current, 1600-ms exposure, performed in PBS-wet gauze). The measured geometrical parameters were used to calculate the bending stress–strain curves for the humeri, where the stress was:

$$\sigma = \frac{FLd}{4I_{\min}},$$

where F being the force, L the loading span, d the anteroposterior diameter, and I_{min} the second moment of inertia from the lateromedial axis ($\pi d^4/64$); and the strain:

$$\varepsilon = \frac{6\delta d}{L^2},$$

where δ being the deflection of the bone due to bending [17]. Stress–strain curves were analyzed with a custom program (Matlab, MathWorks); and the bone elastic (Young's) modulus (E, slope of the linear elastic deformation), yield stress (σy, stress limit between elastic and plastic strain), and ultimate stress (σu, maximum stress) were calculated using the following equations [17]:

$$E = \frac{SL^3}{48I_{\min}}$$

$$\sigma_y = \frac{F_y Lc}{4I_{\min}}$$

$$\sigma_u = \frac{F_u Lc}{4I_{\min}},$$

where c is the radius along the anterior–posterior axis from the humeri cross-sectional centroid.

Vertebrae

Following dissection, the body and posterior elements of the L5 vertebrae were separated using a thin-steel razor blade coated in 0.05-μm diamond suspension. A dermal tool was

then used to make the cranial and caudal ends of the vertebral body flat and parallel for compressive testing. The vertebrae were soaked in PBS and then placed in the compression rig where they were loaded in the cranial–caudal direction. The vertebral force–deflection curves were analyzed with the same custom program (Matlab, MathWorks) used to analyze the curve for the humeri; and bone stiffness, yield force, ultimate force, work to yield were measured [17]. The length of each vertebra was measured with a caliper prior mechanical testing, and the cross-sectional area (CSA) acquired using an environmental scanning electron microscope (ESEM) imaging with backscattering (JEOL JSM-6380LV) in low vacuum mode (pressure of 15 Pa and 15 kV) (Table 1). The CSA was used to calculate the compressive stress–strain curves for the vertebrae, where the stress was

$$\sigma = \frac{F}{A_o}$$

where F being the force and A_o the CSA, and the strain was

$$\varepsilon = \frac{\Delta l}{l_o},$$

where Δl is the change in vertebral length and l_o is the original length.

The elastic modulus, yield, and ultimate stress were calculated as follows [17]:

$$E = \frac{Sl_o}{A_o}$$

$$\sigma_y = \frac{F_y}{A_o}$$

$$\sigma_u = \frac{F_u}{A_o}$$

Fracture Toughness

Left femurs were micro-notched on the posterior surface of the mid-diaphysis with a razor blade irrigated with 0.05-μm diamond suspension, and tested in a three-point bending configuration at a displacement rate of 1 μm/s until fracture, while constantly maintained under PBS hydrated conditions (Instron 5866, Norwood, MA) [18–20]. After a complete break, the fracture surface of the bones was analyzed using an ESEM with simultaneous backscattering (Hitachi S-3400N) in low vacuum mode (pressure of 35 Pa and 25 kV). From these images, geometric characteristics of the bone fracture surface (D, cortical thickness (t), CSA and I_{min}) at the mid-diaphysis were estimated (Table 1). Bone toughness was estimated with the instability method, thus accounting for the contributions to the toughness of both crack initiation and growth. Fracture toughness was computed using the stress-intensity solution for a through-thickness crack in a circular thick-walled cylinder:

$$K_c = F_b \frac{S R_o P_{inst}}{\pi \left(R_o^4 - R_i^4\right)} \sqrt{\pi \theta_{inst} R_m},$$

where F_b is a geometric constant for thick-walled cylinders, P_{inst} is the load at instability, S is the span width, R_m, R_i, and R_o are the mean, inner and outer radius of the bone, respectively, and θ_{inst} is the instability half-crack angle [18–20].

Micro-Computed Tomography

Cortical and trabecular bone were imaged using μCT imaging. Scans were taken along the long axis of the left humeri and CA6 vertebrae using a Scanco μCT 35 system (Scanco Medical, Brüttisellen, Switzerland). Scans were performed in 70% ethanol using 6 μm voxel size, 55 KVp, 0.36° rotation step (180° angular range), and a 400-ms exposure per

view. The Scanco μCT software (HP, DECwindows Motif 1.6) was used for 3D reconstruction and viewing of the images. After 3D reconstruction, volumes were segmented using a global threshold of 0.4 g/c. In cortical bone, we analyzed the total volume (TV), the bone volume (BV), the bone volume density (BV/TV), porosity (Ct.Po = pores volume/TV), cortical area fraction (Ct.Ar/Tt.Ar), mean cortical thickness (Ct.Th), the second moment of inertia along the major and minor axis (I_{max} and I_{min}), the polar moment of inertia (J), tissue mineral density (TMD), and bone mass (TMD/Ct.Po) [21, 22]. For the trabecular bone, BV, TV, BV/TV, connectivity density (Conn-D), trabecular number (Tb.N), trabecular thickness (Tb.Th), trabecular separation (Tb.Sp), and TMD were calculated [21].

Fourier Transform Infrared Imaging Spectroscopy

The composition and distribution of organic and inorganic components of the bone extracellular matrix were evaluated using Fourier transform infrared imaging (FTIRI) spectroscopy. Right femurs were fixed in 90% ethanol and embedded in polymethylmethacrylate (PMMA). Spectra were collected in transmission with a spectral resolution of 4 cm^{-1} and a spatial resolution of 6.25 μm using a Perkin Elmer Spotlight Imaging system from areas of ~300 μm x 500 μm. Sections of 2 μm thickness were scanned to collect five images from intact cortical and five images from trabecular bone. The captured spectra were processed using ISYS software (Spectral Dimensions, Olney, MD), and the atmospheric H20 and CO2 interference were automatically subtracted from all spectra [23, 24]. A linear baseline from 850 to 1850 cm^{-1} was used to normalize the spectra, then PMMA contributions were spectrally subtracted, and the pixels with absorbance

values at 1728 cm^{-1} where masked out using ISYS software. For both cortical and trabecular bone, five bone compositional parameters were examined: the mineral-to-matrix ratio, the carbonate-tophosphate ratio, the mature-to-immature collagen enzymatic crosslinks ratio, the mineral crystallinity, and the acid phosphate substitution. Second derivative spectra were used to define the location of the peaks for intensity calculations. Based on these results, collagen maturity was defined by the relative intensity of 1660/1690 cm^{-1} subbands based on the baseline amide I and amide II 1520–1720 cm^{-1}, crystallinity by the relative intensity of 1030/1020 cm^{-1} subbands, and the acid phosphate substitution by intensities of 1028/1096 cm^{-1} subbands. Mineral-to-matrix ratios were estimated by considering the areas under the baselined peak from 915 to 1215 cm^{-1} over the amide I area (1596–1720 cm^{-1}); carbonate-to-phosphate ratio was instead the area under the peak from 850 to 895 cm^{-1}/915–1215 cm^{-1}. The heterogeneity of these parameters was also analyzed [23–25].

Statistical Analysis

The normal distribution and homogeneity of variance of each variable was analyzed using the Shapiro–Wilk test and the Levene's test, respectively (SPSS, IBM, Somers, NY). Bone strength and toughness, and morphological measures in *Timp-3*$^{-/-}$ and WT bone were compared using the Student's independent *t*-test for variables with normal distributions and the Mann–Whitney rank test for variables with non-normal distributions. Measurements obtained from the FTIRI analysis were evaluated using analysis of variance (one-way nested ANOVA), as we had five measurements per bone. *P*-values smaller than 0.05 were considered significant.

Results

Bone Strength

The humeri and the L5 vertebrae from *Timp-3*$^{-/-}$ mice exhibited significantly lower yield load, ultimate load, work to yield, yield stress, and ultimate stress compared to their WT counterparts (Table 2). Additionally, the *Timp-3*$^{-/-}$ humeri exhibited reduced stiffness. No statistically significant difference between Timp-3−/− and WT mouse bone was found in the elastic modulus.

Fracture Toughness

Fracture toughness testing revealed that the toughness of the *Timp-3*$^{-/-}$ femurs was reduced by a third when compared to the healthy WT femurs (Table 2).

Micro-Computed Tomography

Timp-3$^{-/-}$ bone had a different morphology compared to WT bone (Tables 3, 4). *Timp-3*$^{-/-}$ cortical bone of both humeri and vertebrae exhibited significantly lower TV, BV, BV/TV, Ct.Ar/Tt.Ar, Ct.Th, I_{max}, I_{min}, and J, but a greater Ct.Po, compared to WT bone (Table 3). *Timp-3*$^{-/-}$ trabecular bone from the humeri had a significantly lower TV, Tb.Th, and Tb.Sp compared to normal counterparts, with a greater BV/TV, Conn-D, and Tb.N, than in WT bone (Table 4). *Timp-3*$^{-/-}$ cortical and trabecular bone exhibited lower TMD in the humeri but not in the vertebrae. Bone mass in the *Timp-3*$^{-/-}$ humeri and vertebrae was also reduced when compared to the corresponding WT bone.

Fourier Transform Infrared Imaging Spectroscopy

Analysis of the FTIRI images comparing the *Timp-3*$^{-/-}$ bones to their respective counterparts revealed a significantly lower carbonate-to-phosphate ratio and a significantly greater acid phosphate level in the *Timp-3*$^{-/-}$ cortical and trabecular bone (Fig. 1; Table 5). *Timp-3*$^{-/-}$ trabecular bone also showed an increase in the enzymatic collagen crosslinking ratio.

Heterogeneity of the collagen crosslinking ratio was significantly higher in *Timp-3*$^{-/-}$ cortical and trabecular bone (Table 5). Furthermore, *Timp-3*$^{-/-}$ trabecular bone exhibited a significantly greater heterogeneity of the carbonate-to-phosphate ratio and a significantly lower heterogeneity of the mineral crystallinity compared to WT bone. Neither the mineral-to-matrix ratio nor its heterogeneity differed significantly when the two genotypes were compared.

Discussion

In this study, we investigated the influence of the TIMP-3 gene on bone quality and mechanical integrity of the skeleton of the *Timp-3*$^{-/-}$ mouse model. Our results prove that TIMP-3 is fundamental for regulating and maintaining the correct composition, structure, and mechanics of bone. Understanding how TIMP-3 affects bone integrity is of a great biological and clinical interest for regulating skeletal homeostasis and development.

Our testing revealed compromised mechanical properties of the long bones and vertebrae of the *Timp-3*$^{-/-}$ mice. Inferior yield and ultimate loads were found in *Timp-3*$^{-/-}$bone. Also, stiffness, work to yield, yield and ultimate stress, and fracture toughness were reduced in

Timp-3$^{-/-}$ long bone. Young's modulus values for the *Timp-3*$^{-/-}$ bone demonstrated a tendency to decrease, but the high variance of these values resulted in no statistical significance compared with WT bone. The decrease in the mechanical properties of bone we observed in this study is in agreement with previous works that found compromised tissue quality and function in the respiratory [26], cardiovascular [27], liver [10], and musculoskeletal tissue of *Timp-3*$^{-/-}$ mice [15].

Alterations in the structure and composition of the *Timp-3*$^{-/-}$ bone mice can explain the deficiencies observed in the mechanical properties of the *Timp-3*$^{-/-}$ bone. Our μCT analysis of the bone architecture and mineral density revealed that TIMP-3 deficiency alters both cortical and trabecular bone structure and compromises bone mass. The morphological analysis of *Timp-3*$^{-/-}$ cortical bone revealed a significant decrease in the bone volume, with thinner cortices and higher canal porosity compared with WT bone. *Timp-3*$^{-/-}$ bones were smaller, with a reduced cross-sectional area and altered geometry (I_{max}, I_{min}, and J), in agreement with previous studies conducted on the tibiae of the same mouse strain [15]. The increase in the *Timp-3*$^{-/-}$ cortical bone porosity due to the vascular channels is also in agreement with the increase in angiogenesis typical of these bones [6]. TIMP-3, as all the other TIMPs, is a strong inhibitor of angiogenesis. In particular, TIMP-3 binds directly to VEGF receptor2, blocking the action of VEGF on endothelial cells [1]. Furthermore, MMP-9, regulated by TIMP-3 and produced by osteoclasts, has been identified as a stimulator for angiogenesis in the bone microenvironment [28]. Our results, therefore, suggest that a deficiency in TIMP-3 may directly block inhibition of angiogenesis and further generate an excess of MMP-9, which in turn results in increased bone angiogenesis and vascularization, thus having an effect on the antiangiogenic activity of the other

TIMPs. High intracortical vascular porosity is known to reduce bone resistance to fracture [29] by increasing the stress concentrations around the holes within the bone [22] and by increasing the velocity of crack propagation [19]. Therefore, high bone porosity reduces the mechanical properties of bone and helps explain the decrease in fracture toughness observed here in the *Timp-3*$^{-/-}$ femurs.

Prior research on bone demonstrated that cortical thinning and increased porosity occur when the rate of bone remodeling is altered [30, 31]. In agreement with that, a recent histological analysis of *Timp-3*$^{-/-}$ bone has found an increased osteoclasts number in TIMP-3-deficient bone, with no changes in the osteoblasts number, and no changes in the growth plate area [15]. Thus, it is possible that due to the lack of TIMP-3 in the bone, there is an unregulated MMP, ADAM, and ADAMTS activity in the tissue that leads to an increase in bone remodeling, which may, in turn, decrease cortical thickness and increase bone porosity. Although we did not directly measure bone remodeling in this study, mainly because only fresh frozen mice were available for this study, the possible increase in bone remodeling of the *Timp-3*$^{-/-}$ bone is suggested by the changes in composition of these bones analyzed in this study. Our FTIRI analysis of the *Timp-3*$^{-/-}$ femurs indicates that their cortical and trabecular bone has less carbonate, more acid phosphate, and a more heterogeneous distribution of mature-to-immature enzymatic collagen crosslinks. All these parameters are indicative of increased remodeling in the bone [32–34]. High bone remodeling indeed reduces the carbonate content in the bone, as carbonate is typically where the tissue is not turned over [32], and increases the acid phosphate in the areas of new bone formation and mineral deposition [35]. This is further confirmed by the increase in the heterogeneity of the collagen crosslinking ratio, previously associated with increased

bone remodeling [36]. Carbonate substitutes for phosphate ions in bone (B-type carbonate); thus, the phosphate environment of the mineral is distorted [37]. An increase in crystallinity (crystal size and perfection) would be expected to parallel a loss of carbonate; however, no statistically significant change was seen (1.15 vs 1.16), perhaps because the crystallinity parameter, based on intensities, is less sensitive than the peak area ratio used for carbonate-to-phosphate ratio. Alternatively, since increased acid phosphate substitution (due to new bone formation) would decrease crystallinity, combined these two changes contribute to the constant crystallinity value. Our study thus suggests that an increased remodeling in the *Timp-3*$^{-/-}$ cortical bone creates geometric changes at the bone nanoscale level with more immature (smaller and less perfect) hydroxyapatite crystals and high tissue heterogeneity, which in turn affect the bone architecture at the microscale level and reduce the mass, strength, and toughness of the bone at the organ level. Also, at the trabecular level, changes in the composition of the *Timp-3*$^{-/-}$ bone result in the altered micro-architecture, characterized by a reduced total bone volume with an increased volume density and more, thinner, highly connected, and closely packed trabeculae: a typical configuration of a bone with high remodeling. Interestingly, the trabecular configuration we observed in the *Timp-3*$^{-/-}$ mice is not due to improper growth plate cartilage degradation [15] rather our results suggest collagenases are predominantly responsible for altered *Timp-3*$^{-/-}$ bone architecture through imbalanced bone remodeling.

Previous studies examining bone matrix in the presence of increased MMP-1, -2, -8, -9, -14, and -16 activities found a higher bone remodeling due to excessive collagen degradation, generating skeletal abnormalities and deformities [28, 38–41]. Both ADAMs and ADAMTS could also influence the rate of bone remodeling [42–44]. In particular,

ADAM-10 and ADAM-12 play a role in bone in influencing human peripheral blood mononuclear cells to differentiate into osteoblasts and osteoclasts [42]. Inhibition of ADAM-15 activity can increase osteoblast proliferation and function and result in higher bone mass [43]. Furthermore, ADAMTS-18 deletion significantly correlated to increased osteoclastogenesis and osteoblastogenesis [44]. It is also possible that common substrates between the TIMPs allow for other TIMPs to regulate metalloproteinases activity in absence of TIMP-3. For example, the increased bone formation with highly connected and closely spaced trabeculae we observed in the *Timp-3*$^{-/-}$ mice was previously found in the skeleton of MMP-13 Null mice [45]. MMP-13 plays a role in remodeling the cartilage matrix in endochondral ossification, vascularization, and chondroclast recruitment, and the change observed in trabecular bone has been related to improper cartilage degradation with hypertrophic chondrocytes and osteoblasts due to the lack of MMP-13 [39, 45]. With a TIMP-3 deficiency, we would expect instead an overabundance of MMP-13. Thus, it is possible that either TIMP-3 is less effective than other TIMPs in regulating MMP-13 or that the actions of TIMP-3 are taken over by other TIMPs and without this redundancy, the phenotype of the *Timp-3*$^{-/-}$mice could even be more severe. Future studies are required to elucidate the relationship between the TIMPs and MMPs, ADAMs, and ADAMTSs, to reveal which enzymes are directly involved in the changes observed in the *Timp-3*$^{-/-}$ bone. This study has some limitations that need to be pointed out. First, because the animals were not double-labeled, we were unable to do histomorphometry to confirm the altered remodeling. Secondly, we did not measure the composition of all bones (but only femurs), nor of an entire bone, but rather selected intact cortical bone and intact trabeculae and considered their averages and distributions, rather than a unique site (e.g., adjacent to newly

deposited bone). This, in a sense, is analogous to measuring the chemical composition of multiple aliquots of cortical or cancellous bones from several different animals, thus the need to use a nested statistical analysis to account for measurements from the same bones.

Conclusions

This study demonstrates that TIMP-3 plays a fundamental role in determining and maintaining bone quality and integrity, regulating both cortical and trabecular bone. The lack of TIMP-3 generates smaller bones with thin and highly porous cortex and dense, highly connected and closely packed, thin trabeculae. Composition is also altered in *Timp-3*$^{-/-}$ bone, with smaller, immature, and less perfect crystals. This compromised structure and composition results in the inferior mechanical properties of the *Timp-3*$^{-/-}$ bone. This study therefore proves that TIMP-3 is a critical component for maintaining healthy bone, enabling its matrix to properly mature, generate, and maintain optimal compositional, structural, and mechanical properties. Our results open the way to further studies for a thorough investigation of the relations between TIMP-3, and MMP, ADAM, ADAMTS activity, and bone properties, and their relation with the compromised quality of other tissue in *Timp-3*$^{-/-}$ mice. These future studies will eventually lead to the development of treatments for diseases related to abnormal TIMP-3, MMPs, ADAMs, and ADAMTSs activity, with the ultimate aim to improve tissue quality and quantity, and regain healthy mechanical properties in bone as well as in other body tissues.

Acknowledgements

The authors are grateful for the provision of *Timp-3−/−* mice by Dr. Rama Khokha (Toronto, Canada). This study was funded by the Florida Institute of Technology and partly supported by Arthritis Research UK (ARUK) grant 20039 awarded to GB and by grants awarded to AAP by ARUK (20581) and Biotechnology and Biological Sciences Research Council (BB/J003727/1).

Compliance with Ethical Standards

Conflict of interest:

The authors Brendyn Miller, Lyudmila Spevak, Lyudmila Lukashova, Behzad Javaheri, Andrew A. Pitsillides, Adele Boskey, George Bou-Gharios, and Alessandra Carriero declare that they have no conflict of interest.

Human and Animal Rights and Informed Consent:

Mice were maintained under standard laboratory conditions and experiments were conducted in compliance with the ARRIVE (Animal Research: Reporting of In Vivo Experiments) guidelines for reporting. Briefly, mice were housed up to 4 per cage in polypropylene cages with wood chip and paper bedding and provided standard rodent maintenance diet and water ad libitum throughout the study. All procedures complied with the UK Animals (Scientific Procedures) Act 1986 and were reviewed and approved by UK Home Office and local ethics committee.

References

1. Brew K, Nagase H (2010) The tissue inhibitors of metalloproteinases (TIMPs): an ancient family with structural and functional diversity. Biochimica et Biophysica Acta (BBA)-Mol Cell Res 1803(1):55–71
2. Zhao H et al (2004) Differential inhibition of membrane type 3 (MT3)-matrix metalloproteinase (MMP) and MT1-MMP by tissue inhibitor of metalloproteinase (TIMP)-2 and TIMP-3 regulates pro-MMP-2 activation. J Biol Chem 279(10):8592–8601
3. Apte SS, Parks WC (2015) Metalloproteinases: A parade of functions in matrix biology and an outlook for the future. Matrix Biol 44:1–6
4. Maretzky T et al (2009) Characterization of the catalytic activity of the membrane-anchored metalloproteinase ADAM15 in cellbased assays. Biochem J 420(1):105–113
5. Shen Y et al (2010) Tissue inhibitor of metalloproteinase-3 (TIMP-3) regulates hematopoiesis and bone formation in vivo. PLoS ONE 5(9):e13086
6. Cruz-Munoz W, Kim I, Khokha R (2006) TIMP-3 deficiency in the host, but not in the tumor, enhances tumor growth and angiogenesis. Oncogene 25(4):650–655
7. Verstappen J, Von den Hoff JW (2006) Tissue inhibitors of metalloproteinases (TIMPs): their biological functions and involvement in oral disease. J Dent Res 85(12):1074–1084
8. Weber BH et al (1994) Mutations in the tissue inhibitor of metalloproteinases-3 (TIMP3) in patients with Sorsby's fundus dystrophy. Nat Genet 8(4):352–356
9. Sahebjam S, Khokha R, Mort JS (2007) Increased collagen and aggrecan degradation with age in the joints of Timp3−/− mice. Arthritis Rheumatism 56(3):905–909
10. Mohammed FF et al (2004) Abnormal TNF activity in Timp3−/− mice leads to chronic hepatic inflammation and failure of liver regeneration. Nat Genet 36(9):969–977
11. Janssen A et al (2008) Abnormal vessel formation in the choroid of mice lacking tissue inhibitor of metalloprotease-3. Investig Ophthalmol Vis Sci 49(7):pp. 2812–2822
12. Fedak PW et al (2004) TIMP-3 deficiency leads to dilated cardiomyopathy. Circulation 110(16):2401–2409
13. Gill SE et al (2003) A null mutation for Tissue Inhibitor of Metalloproteinases-3 (Timp-3) impairs murine bronchiole branching morphogenesis. Dev Biol 261(2):313–323
14. Federici M et al (2005) Timp3 deficiency in insulin receptor–haploinsufficient mice promotes diabetes and vascular inflammation via increased TNF-α. J Clin Invest 115(12):3494–3505
15. Javaheri B et al (2016) Deficiency and also transgenic overexpression of Timp-3 both lead to compromised bone mass and architecture in vivo. PLoS ONE 11(8):e0159657
16. Leco KJ et al (2001) Spontaneous air space enlargement in the lungs of mice lacking tissue inhibitor of metalloproteinases-3 (TIMP-3). J Clin Invest 108(6):817–829
17. Turner CH, Burr DB (1993) Basic biomechanical measurements of bone: a tutorial. Bone 14(4):595–608 18. Ritchie R et al (2008) Measurement of the toughness of bone: a tutorial with special reference to small animal studies. Bone 43(5):798–812
19. Carriero A et al (2014) How tough is brittle bone? Investigating osteogenesis imperfecta in mouse bone. J Bone Miner Res 29(6):1392–1401
20. Carriero A et al (2014) A methodology for the investigation of toughness and crack propagation in mouse bone. J Mech Behav Biomed Mater 39:38–47

21. Bouxsein ML et al (2010) Guidelines for assessment of bone microstructure in rodents using micro–computed tomography. J Bone Miner Res 25(7):1468–1486
22. Carriero A et al (2014) Altered lacunar and vascular porosity in osteogenesis imperfecta mouse bone as revealed by synchrotron tomography contributes to bone fragility. Bone 61:116–124
23. Boskey AL et al (2013) The kidney sodium–phosphate co-transporter alters bone quality in an age and gender specific manner. Bone 53(2):546–553
24. Verdelis K et al (2008) DSPP effects on in vivo bone mineralization. Bone 43(6):983–990
25. Paschalis EP et al (2015) Fourier transform Infrared spectroscopic characterization of mineralizing type I collagen enzymatic trivalent cross-links. Calcif Tissue Int 96(1):18–29
26. Martin EL et al (2007) Lung mechanics in the TIMP3 null mouse and its response to mechanical ventilation. Exp Lung Res 33(2):99–113
27. Hammoud L et al (2011) Deficiency in TIMP-3 increases cardiac rupture and mortality post-myocardial infarction via EGFR signaling: beneficial effects of cetuximab. Basic Res Cardiol 106(3):459–471
28. Bruni-Cardoso A et al (2010) Osteoclast-derived matrix metalloproteinase-9 directly affects angiogenesis in the prostate tumor– bone microenvironment. Mol Cancer Res 8(4):459–470
29. Ural A, Vashishth D (2007) Effects of intracortical porosity on fracture toughness in aging human bone: a μCT-based cohesive finite element study. J Biomech Eng 129(5):625–631
30. Shigdel R et al (2015) Bone turnover markers are associated with higher cortical porosity, thinner cortices, and larger size of the proximal femur and non-vertebral fractures. Bone 81:1–6
31. Bell K et al (1999) Intracapsular hip fracture: increased cortical remodeling in the thinned and porous anterior region of the femoral neck. Osteoporos Int 10(3):248–257
32. Isaksson H et al (2010) Infrared spectroscopy indicates altered bone turnover and remodeling activity in renal osteodystrophy. J Bone Miner Res 25(6):1360–1366
33. Malluche HH et al (2012) Differences in bone quality in lowand high-turnover renal osteodystrophy. J Am Soc Nephrol 23(3):525–532
34. Boskey AL (2013) Bone composition: relationship to bone fragility and antiosteoporotic drug effects. Bonekey Rep 2:447
35. Spevak L et al (2013) Fourier transform infrared spectroscopic imaging parameters describing acid phosphate substitution in biologic hydroxyapatite. Calcif Tissue Int 92(5):418–428
36. Donnelly E et al (2012) Reduced cortical bone compositional heterogeneity with bisphosphonate treatment in postmenopausal women with intertrochanteric and subtrochanteric fractures. J Bone Miner Res 27(3):672–678
37. Marisa ME et al (2016) Paracrystalline disorder from phosphate ion orientation and substitution in synthetic bone mineral. Inorg Chem 55(23):12290–12298
38. Ohuchi E et al (1997) Membrane type 1 matrix metalloproteinase digests interstitial collagens and other extracellular matrix macromolecules. J Biol Chem 272(4):2446–2451

39. Inada M et al (2004) Critical roles for collagenase-3 (Mmp13) in development of growth plate cartilage and in endochondral ossification. Proc Natl Acad Sci U S A 101(49):17192–17197
40. Garnero P et al (2003) The type I collagen fragments ICTP and CTX reveal distinct enzymatic pathways of bone collagen degradation. J Bone Miner Res 18(5):859–867
41. Holmbeck K et al (1999) MT1-MMP-deficient mice develop dwarfism, osteopenia, arthritis, and connective tissue disease due to inadequate collagen turnover. Cell 99(1):81–92
42. Verrier S et al (2004) ADAM gene expression and regulation during human osteoclast formation. Bone 35(1):34–46
43. Marzia M et al (2011) Lack of ADAM15 in mice is associated with increased osteoblast function and bone mass. Biol Chem 392(10):877–885
44. Uddin SM, Liu B, Liu C, Li ZD (2014) Adamts 18 A novel regulator of bone remodeling. In: Annual meeting of the orthopaedic research society, 2014. New Orleans
45. Stickens D et al (2004) Altered endochondral bone development in matrix metalloproteinase 13-deficient mice. Development 131(23):5883–5895

Figures

Figure 1: FTIRI of cortical and trabecular bone of one representative femur from WT and one from *Timp-3*$^{-/-}$ bone (* indicates p < 0.05, ** indicates $p < 0.01$, and *** indicates $p < 0.001$)

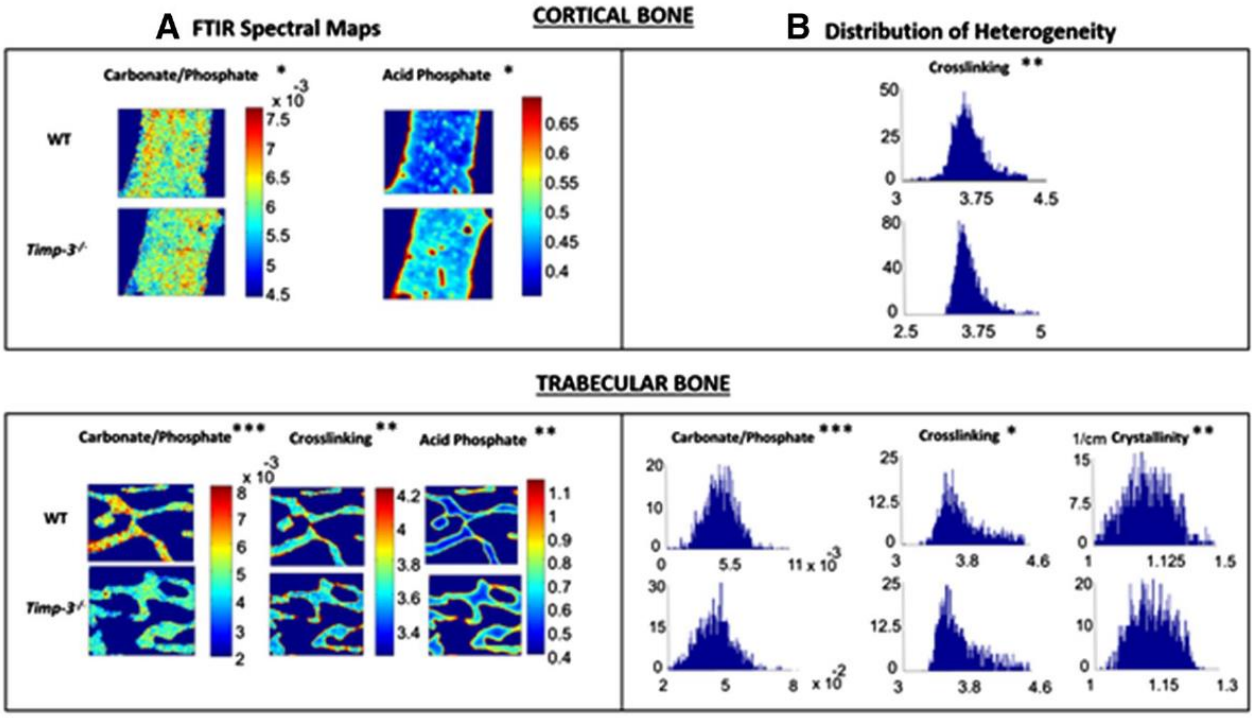

Table 1: Cortical bone geometric properties of the humeri, L5 vertebrae, and femurs of WT and Timp-3−/− mice indicate that *Timp-3*$^{-/-}$ bones are smaller than their WT counterparts (* indicates $p < 0.05$, ** indicates $p < 0.01$, and *** indicates $p < 0.001$)

Geometric parameter	WT (N=6)
Humeri	
Diameter (mm)	1.47 ± 0.12
Cross-sectional area (mm^2)	1.04 ± 0.12
Second moment of area (mm^4)	0.17 ± 0.03
L5 Vertebrae	
Length (mm)	2.55 ± 0.30
Cross-sectional area (mm^2)	2.34 ± 0.79
Femurs	
Diameter (mm)	1.62 ± 0.06
Average thickness (mm)	0.26 ± 0.02
Cross-sectional area (mm^2)	1.07 ± 0.09
Second moment of area (mm^4)	0.16 ± 0.02 0.12

Table 2: Mechanical and material properties of WT and *Timp-3*$^{-/-}$ mice cortical bone

Mechanical parameter	Cortical bone			
	Humeri		L5 Vertebrae	
	WT (N=6)	*Timp-3*$^{-/-}$ (N=9)	WT (N=6)	*Timp-3*$^{-/-}$ (N=9)
Stiffness (N/mm)	94.32 ± 11.10	43.85 ± 13.73***	90.28 ± 34.08	63.78 ± 31.94
Yield load (N)	10.40 ± 2.05	4.50 ± 1.28***	10.35 ± 2.37	5.36 ± 2.56**
Ultimate load (N)	13.33 ± 1.52	6.42 ± 1.39***	12.92 ± 2.50	6.39 ± 3.04**
Work to yield (mJ)	0.65 ± 0.25	0.25 ± 0.10***	0.70 ± 0.32	0.27 ± 0.19**
Work to fracture (mJ)	2.65 ± 0.67	2.20 ± 0.99	-	-
Elastic modulus (GPa)	8.66 ± 1.55	6.60 ± 2.69	0.11 ± 0.07	0.07 ± 0.03
Yield stress (MPa)	102.80 ± 12.20	59.85 ± 15.84***	4.67 ± 1.42	2.52 ± 1.20**
Ultimate stress (MPa)	133.12 ± 15.37	86.48 ± 19.35***	5.93 ± 1.42	3.00 ± 1.41**
	Femurs			
	WT (N = 6)	*Timp-3*$^{-/-}$ (N=9)		
Fracture toughness (Mpa √ m)	6.36 ± 0.68	4.28 ± 0.31**		

Mechanical properties of bone were found to be altered by TIMP-3 deficiency as both the *Timp-3*−/− humeri and the L5 vertebrae exhibited significantly reduced yield and ultimate load, work to yield, yield stress, and ultimate stress measurements

The stiffness of the *Timp-3*−/− humeri was also significantly reduced. The Young's modulus measurements were instead not significantly different, mostly because of high variance within the groups

The fracture toughness of the *Timp-3*−/− bone, measured in terms of stress intensity, Kc, was significantly reduced, indicating that the *Timp-3*−/− bone had a reduced resistance to crack propagation
(* indicates $p < 0.05$, ** indicates $p < 0.01$, and *** indicates $p < 0.001$)

Table 3: Structural analysis of the cortical bone in the humeri and CA6 vertebrae of WT and *Timp-3*$^{-/-}$ bone indicates that the TIMP-3 deficiency alters the structural properties of cortical bone

μCT parameter	Cortical bone			
	Humeri		Vertebrae	
	WT (N = 6)	*Timp-3*$^{-/-}$ (N = 9)	WT (N=6)	*Timp-3*$^{-/-}$ (N = 9)
TV (mm^3)	1.41 ± 0.08	1.11 ± 0.07***	1.20 ± 0.11	1.01 ± 0.09*
BV (mm^3)	0.83 ± 0.04	0.6 ± 0.04***	0.79 ± 0.06	0.56 ± 0.04***
BV/TV (%)	59 ± 1	54 ± 2***	66 ± 2	56 ± 3***
Ct.Po (%)	5.04 ± 1.42	8.51 ± 0.51**	7 ± 1	16 ± 5**
Ct.Ar/Tt.Ar (%)	59 ± 1	54 ± 2***	66 ± 2	56 ± 3***
Ct.Th (mm)	0.20 ± 0.00	0.15 ± 0.01***	0.18 ± 0.01	0.11 ± 0.02**
I_{max} (mm^4)	0.09 ± 0.01	0.05 ± 0.07***	0.13 ± 0.03	0.09 ± 0.02**
I_{min} (mm^4)	0.06 ± 0.01	0.03 ± 0.01***	0.12 ± 0.02	0.07 ± 0.01***
J (mm^4)	0.14 ± 0.01	0.08 ± 0.01***	0.26 ± 0.05	0.16 ± 0.03**
TMD (mg/cm^{-3})	1124.91 ± 4.83	1063.95 ± 16.41***	938.49 ± 12.62	892.49 ± 72.33
Bone Mass (mg)	236.50 ± 56.35	125.35 ± 7.83**	132.48 ± 12.07	62.08 ± 25.64***

Both the *Timp-3*$^{-/-}$ humeri and the CA6 vertebrae had reduced total volume (TV), bone volume (BV), bone volume density (BV/TV), thickness (Ct.Th), moments of inertia (Imax, Imin, J), tissue mineral density (TMD), and overall bone mass

Both types of bones in TIMP-3 deficient mice also exhibited higher cortical porosity (Ct.Po)

* indicates $p < 0.05$, ** indicates $p < 0.01$, and *** indicates $p < 0.001$

Table 4: Structural analysis of the trabecular bone in the humerus of WT and *Timp-3*$^{-/-}$ bone

μCT parameter	Humeral trabecular bone	
	WT (N = 6)	*Timp-3*$^{-/-}$ (N = 9)
TV (mm^3)	1.57 ± 0.05	1.16 ± 0.18***
BV (mm^3)	0.19 ± 0.02	0.16 ± 0.03
BV/TV (%)	12 ± 1	14 ± 1*
Conn-Dens. (mm^{-3})	294.13 ± 38.84	552.83 ± 113.67***
Tb.N (mm^{-1})	4.47 ± 0.32	6.15 ± 0.67***
Tb.Th (mm)	0.04 ± 0.00	0.03 ± 0.00***
Tb.Sp (mm)	0.23 ± 0.02	0.16 ± 0.02***
TMD (mm^{-3})	914.41 ± 8.24	873.81 ± 18.99**

Bone volume density (BV/TV), connectivity density (Conn.Dens), and trabecular number (Tb.N) were significantly increased in the trabecular bone of the TIMP-3-deficient mice

Timp-3$^{-/-}$ trabecular bone had also a significant decrease in the total volume (TV), trabecular thickness (Tb.Th), trabecular separation (Tb.Sp), and tissue mineral density (TMD)

* indicates $p < 0.05$, ** indicates $p < 0.01$, and *** indicates $p < 0.001$

Table 5: FTIR parameters for cortical and trabecular bone of WT and *Timp-3*$^{-/-}$ femurs

FTIR parameter	Cortical bone		Trabecular bone	
	WT (N=6)	*Timp-3*$^{-/-}$ (N = 9)	WT (N=6)	*Timp-3*$^{-/-}$ (N = 9)
Mineral/matrix ratio	6.66 ± 0.56	6.97 ± 0.89	5.57 ± 0.45	5.87 ± 0.41
Carbonate/phosphate ratio (10^{-3})	6.20 ± 0.50	5.50 ± 0.80*	5.90 ± 0.80	4.30 ± 0.50***
Crosslink ratio	3.77 ± 0.13	3.87 ± 0.19	3.96 ± 0.20	4.35 ± 0.24**
Crystallinity	1.20 ± 0.03	1.20 ± 0.04	1.15 ± 0.02	1.16 ± 0.03
Acid phosphate	0.49 ± 0.02	0.52 ± 0.05*	0.63 ± 0.04	0.71 ± 0.05**
Mineral/matrix heterogeneity	2.14 ± 0.59	2.27 ± 0.61	2.51 ± 0.49	2.81 ± 0.65
Carbonate/phosphate heterogeneity (10^{-3})	2.10 ± 0.1	2.20 ± 0.20	2.60 ± 0.30	3.30 ± 0.40***
Crosslink heterogeneity	0.42 ± 0.03	0.55 ± 0.10**	0.50 ± 0.08	0.85 ± 0.30*
Crystallinity heterogeneity (10^{-2})	12.97 ± 1.53	12.42 ± 2.05	19.07 ± 1.71	16.72 ± 0.81**

Measurements of the WT and *Timp-3*$^{-/-}$ cortical bone revealed that there was a 12.7% reduction of carbonate substitution in the hydroxyapatite crystals, a 7.4% increase in the amount of acid phosphate, and a 23.5% increase in the heterogeneity of the mature-to-immature collagen crosslinking ratio in the *Timp-3*$^{-/-}$ bone matrix. The FTIRI measurements of the WT and *Timp-3*$^{-/-}$ trabecular bone demonstrated a 37.2% decrease in carbonate substitution in the hydroxyapatite crystals, an 8.8% increase in the collagen enzymatic crosslinking ratio, and an 11.1% increase in the acid phosphate ratio

Analysis of the compositional heterogeneity of *Timp-3*$^{-/-}$ trabecular bone demonstrated a 21.2% increase in the carbonate-to-phosphate ratio heterogeneity, a 41% increase in the collagen enzymatic crosslinking ratio heterogeneity, and a 14.1% decrease in the crystallinity heterogeneity of the hydroxyapatite crystals in the matrix

* indicates $p < 0.05$, ** indicates $p < 0.01$, and *** indicates $p < 0.001$